Mixed metal-antimony oxide nanocomposites: low pH water oxidation electrocatalysts with outstanding durability at ambient and elevated temperatures

Sibimol Luke,[†,§,‖] Manjunath Chatti,[⊥,‡] Asha Yadav,[#,‡] Brittany V. Kerr,[▽] Jiban Kangsabanik,[#] Tim Williams,[○] Pavel V. Cherepanov,[⊥] Akshat Tanksale,[‖] Bernt Johannessen,[△] Douglas R. MacFarlane,[⊥,|] Rosalie K. Hocking,[▽,*] Aftab Alam,[#,*] Aswani Yella,[§,*] Alexandr N. Simonov[⊥,|,*]

[†] IITB-Monash Research Academy, IIT Bombay, Mumbai 400076, India

[§] Department of Metallurgical Engineering and Materials Science, IIT Bombay, Powai, Mumbai 400076, India

[‖] Department of Chemical Engineering, Monash University, Clayton, Victoria 3800, Australia

[⊥] School of Chemistry, Monash University, Clayton, Victoria 3800, Australia

[#] Department of Physics, IIT Bombay, Powai, Mumbai 400076, India

[▽] Department of Chemistry and Biotechnology, Swinburne University of Technology, Hawthorn, Victoria 3800, Australia

[○] Monash Centre for Electron Microscopy, Clayton, Victoria 3800, Australia

[△] Australian Synchrotron, Clayton, Victoria 3168, Australia

[|] ARC Centre of Excellence in Electromaterials Science, Monash University, Clayton, Victoria 3800, Australia

*Corresponding authors:

Rosalie K. Hocking: rhocking@swin.edu.au

Aftab Alam: aftab@phy.iitb.ac.in

Aswani Yella: aswani.yella@iitb.ac.in

Alexandr N. Simonov: alexandr.simonov@monash.edu

Proton-exchange membrane water electrolysers provide many advantages for the energy-efficient production of H_2, but the current technology relies on high loadings of expensive iridium at the anodes, which are often unstable in operation. To address this, the present work scrutinises the properties of antimony-metal (Co, Mn, Ni, Fe, Ru) oxides synthesised as flat thin films by a solution-based method for the oxygen evolution reaction in 0.5 M H_2SO_4. Among the non-noble-metal catalysts, only cobalt-antimony and manganese-antimony oxides demonstrate high stability and reasonable activity under ambient conditions, but slowly lose activity at elevated temperatures. The ruthenium-antimony system is highly active, requiring an overpotential of 0.39 ± 0.03 and 0.34 ± 0.01 V to achieve 10 mA cm^{-2} at 24 ± 2 and 80 °C, respectively, and remaining remarkably stable during one-week tests at 80 °C. The *S*-number for this catalyst is higher than that for the high-performance benchmark Ir-based systems. Density functional theory analysis and physical characterisation reveal that this high stability is supported by the enhanced hybridisation of the oxygen p- and metal d-orbitals induced by antimony, and can arise from two distinct structural scenarios: either formation of an antimonate phase, or nanoscale intermixing of metal and antimony oxide crystallites.

1. Introduction

Water electrolysers based on a proton-exchange membrane (PEM) electrolyte are currently seen as the preferred technology for the production of *green* hydrogen from renewables.[1] Double digit megawatt PEM plants are already available and even larger installations are planned.[2] Recent breakthroughs in the design of bipolar plates and cathode catalysts for the PEM electrolysers now throw a spotlight on the membrane and anode electrocatalysts as the components requiring further significant cost-efficiency improvements.[3] Catalysts for the oxygen evolution reaction (OER) are particularly problematic in essentially all key aspects – price, availability, activity and stability. While iridium oxides provide perhaps the best combination of the activity and stability among known monometallic catalysts,[1a] there is not enough of this exceptionally rare metal currently available to us to bring the PEM water electrolysis to the TW scale.[4] Moreover, both theoretical and extensive experimental studies reveal the unavoidable degradation of iridium-based OER catalysts even under ambient conditions,[5] and especially in industrially relevant high-temperature tests,[6] which is among the reasons for the comparatively high loadings of Ir in the anodes of PEM electrolysers.

Alternative OER catalysts based on more abundant and cheaper elements exist, in particular lead(IV)-based oxides developed through decades of research on the metal electrowinning anodes,[7] though their specific activity is significantly lower than that of iridium systems.[8] Among other non-noble metal options, the obvious candidates are oxides of manganese, cobalt, nickel and iron, which have been widely investigated as OER catalysts for the alkaline and near neutral conditions.[9] Monometallic oxides of Mn and Co have also been examined for applications in acidic environment, and in contrast to Ni and Fe which immediately dissolve,[10] relatively stable performance for several hours was demonstrated.[11] However, eventual degradation and essentially complete loss of activity is unavoidable. A noble alternative to iridium is also known – ruthenium oxides are reported to be at least as active OER catalysts.[10] While the amount of Ru in the Earth's crust is only slightly higher than that of Ir[12] and it continues to rise in price, ruthenium is still more than five-fold cheaper,[13] is

easier to refine and is produced on an order of magnitude higher scale.[14] However, rapid degradation of RuO_2 anodes is again a major issue.[15]

Overall, it is highly unlikely that any monometallic oxide can provide an optimal combination of characteristics required to be a high-performance OER catalyst. In contrast, new materials with improved activity and/or stability emerge from the exploration of multielement oxide systems that sometimes combine the properties of individual compounds or exhibit distinct properties of their own. In the context of the design of catalysts for the low pH OER, successful approaches often emerge from combining a catalytically active oxide with the one that is highly stable under operating conditions to enable improved long-term operation with decreased losses in activity. This strategy has been broadly adopted for many years in the research on the electrowinning anode catalysts using PbO_2 as a "matrix" that stabilises oxides of cobalt, manganese, silver and other metals.[7, 16] The same approach is now also applied in the design of anode catalysts for PEM water electrolysers. Improved electrochemical activity and durability during the OER in acidic solutions has been reported when catalytically active metals have been combined with the oxides of Ta^{IV},[17] Sn^{IV},[17b, 18] Ti^{IV},[19] Pb^{IV},[20] Y^{III},[21] Cr^{IV},[22] and also Sb^{V}.[23]

Antimony oxides (SbO_x) are of a particular interest in this context. The thermodynamic stability of SbO_x under the low pH OER conditions,[24] electrical conductivity,[25] along with abundance and availability of Sb[26] render these compounds a suitable structural component for acid-stable water oxidation electrocatalysts. Antimony oxides have been used as stabilising interlayers and components in robust electrowinning anodes,[27] and have recently been also introduced to studies of OER catalysts for acidic water electrolysers. In particular, the research teams of Gregoire[23b, 28] and Lewis[23a, 29] both reported promising activity and improved stability in operation of antimonates of manganese and nickel. More recent work also described cobalt antimonate OER catalysts.[30] Thus, the stability of transition metal oxides during oxidation of acidic water can be improved *via* combination with the highly promising SbO_x matrix. In the case of Ru, this can also reduce the noble

metal loading and thereby the cost. However, the catalysts of this type are currently underexplored and have only recently gained an increased attention.

In the search for highly active, and genuinely stable catalysts under practical operating conditions, the core aim of the present work is the investigation of the electrocatalytic activity and stability of mixed metal-antimony oxides towards the oxidation of acidic water. Specific emphasis is put on the stability, which is rarely assessed rigorously in the current literature, *viz.* the experiments are commonly limited to several hours and ambient temperature conditions only. Moreover, even such mild conditions cause continuous degradation of many catalysts, which sometimes remains underestimated when the stability data are recorded and presented in the galvanostatic mode. Herein, the initial tests were also undertaken under ambient conditions to identify the most promising catalysts, which were further investigated at elevated temperatures to assess and demonstrate the genuine suitability of antimony-metal oxides for operation under the conditions relevant to the PEM electrolysers. In-depth electrochemical and physical characterisation of the catalysts before and after exhaustive electrocatalytic tests coupled to the density functional theory (DFT) calculations reveal new insights into the origins of the stability of metal-antimony oxide OER catalysts on the structural and atomistic levels.

2. Results and Discussion

All materials in this work were synthesised *via* annealing of precursor salts deposited from their solutions onto nominally flat glass supports covered with a thin conductive layer of F-doped SnO_2 (FTO). While sputtering and similar advanced techniques provide a better control over the morphology and composition, our choice over the much simpler drop-casting/annealing fabrication protocol was motivated by the ease of the future optimisation of this approach for the creation of high-surface area catalysts of applied significance. All electrochemical tests were undertaken in 0.5 M H_2SO_4 with measured pH of 0.3 (at ambient temperature). All galvanostatic data are presented below after manual post-correction for ohmic losses using the uncompensated (R_u) values measured

by the electrochemical impedance spectroscopy. However, the correction was generally not applied to voltammograms, where currents cannot be always confidently attributed to the stationary catalytic process only. Extended details on the methods and procedures used in this work are provided in Experimental Section.

2.1 Electrocatalytic activity under ambient conditions

Individual metal oxides (MO_x) considered herein, *viz.* RuO_x, CoO_x, MnO_x, NiO_x and FeO_x, as well as SbO_x, were not expected to be high-performance OER catalysts of independent interest, but their properties were briefly examined to understand relevant differences in the key performance parameters that are likely to affect those of the corresponding metal-antimony oxides. X-ray diffraction (XRD) and scanning electron microscopic (SEM) analysis of the as-prepared MO_x and SbO_x indicate that the materials were dominated by single oxide phases RuO_2, Co_3O_4, Mn_2O_3, NiO, Fe_2O_3, and Sb_2O_4 (**Figure S1**) of variable morphology (**Figure S2**). Tests of MO_x and SbO_x as OER catalysts confirmed their either limited stability (RuO_2, Co_3O_4, NiO and Fe_2O_3) or activity (Mn_2O_3 and Sb_2O_4) (**Figures S3-S5** and attached comments).

Further studies focused on mixed metal-antimony oxides, which are referred to as $[M+Sb]O_y$. These catalysts were synthesised with a 1:1 molar metal:antimony precursor ratio, unless stated otherwise, but the actual composition during the OER is different due to the unavoidable corrosion in acidic solutions. The degree of this corrosion for the selected key materials was quantified (**Table 1**) and is discussed later in the text.

Table 1. Relative loss of metals and antimony from catalysts (at.%)[a] during the OER in stirred 0.5 M H_2SO_4 and corresponding *S*-numbers.[b]

Catalyst	24 ± 2 °C [c]		80 °C [d]	
	Metal	Sb	Metal	Sb
[Mn+Sb]O_y	21	17		
	1.1 × 10⁴		Not analysed	
[Co+Sb]O_y	15	26		
	1.5 × 10⁴			
[Ru+Sb]O_y	1	37	3	47
	1.6 × 10⁵		*6.0 × 10⁵*	

[a] Calculation based on the amount of metal and Sb deposited onto electrodes (1 μmol cm^{-2} each) and the amounts measured in solutions after the OER tests by ICP-OES. [b] Provided in italics and calculated as a molar ratio between the amount of O_2 evolved and the amount of catalytic metal dissolved. [c] 10 mA cm^{-2} for 24 h and then 2.03 and 1.93 V vs. RHE for 0.5 h at each potential. [d] 10 mA cm^{-2} for 192 h and then 2.03 and 1.93 V vs. RHE for 0.5 h at each potential.

First, we exclude Ni- and Fe-based systems from detailed analysis, as these materials rapidly degraded under the OER conditions (**Figure S6 and S7**). Attempts to improve their performance through variations in the metal : antimony ratios and annealing temperature were not successful. The effect of the latter parameter was also briefly considered for the much better performing Co-, Mn- and Ru-Sb oxide catalysts. The best results were always obtained at 600 °C **(Figure S8**), which is the highest value we could use due to thermal instability of FTO.[31] Hence, all results discussed here in the main text of the paper were obtained with the catalysts synthesised at 600 °C.

Voltammetric assessment of the initial OER catalytic activity of CoO_x and [Co+Sb]O_y revealed lower performance of the latter (**Figure** S3a and **1a**), which is likely associated with the reduced amount of the active cobalt oxide surface species, as also measured by cyclic voltammetry (*cf.* **Figures** S5a and **S9a**). Subsequently recorded chronopotentiograms reveal the significant initial degradation of the cobalt-antimony-modified electrode, though more importantly [Co+Sb]O_y catalysts do not completely lose their activity and sustain a current density of 10 mA cm^{-2} at a reasonable overpotential (Figure 1b). The choice of 10 mA cm^{-2} for stability measurements herein is justified by the essentially flat, very low-surface area morphology of the employed catalyst layers. The duration of the initial drop increased with an increase in the Co : Sb ratio used for the synthesis, while the best stabilised

activity was demonstrated by the catalysts prepared with equimolar amounts of Co and Sb (**Figure S10**). This type of [Co+Sb]O_y demonstrated stable water oxidation at 10 mA cm^{-2} at a well-reproducible IR_u-corrected overpotential of 0.769 ± 0.010 V (**Figures** 1b and **S11**). Subsequent potentiostatic tests at 2.03 and 1.93 V *vs.* RHE also did not reveal further significant losses in the catalytic activity (Figure 1c). A plausible explanation of the rapid initial loss of the performance is provided in the following section, while at this stage we conclude that [Co+Sb]O_y exhibits a reasonable short-term stability during the OER at low pH and ambient temperature, yet its catalytic activity is not high.

In contrast to the cobalt-based materials, combination of Mn with Sb produced a very significant improvement in the OER catalytic activity with respect to monometallic MnO_x (Figure S3b and 1a). The [M+Sb]O_y catalysts were also able to maintain the initial performance during 24 h galvanostatic tests (Figure 1b). Variations in the Mn to Sb precursor ratio revealed that the manganese-rich materials (Mn : Sb = 2 : 1) suffer slow deterioration in performance (**Figure S12**), which was also recently reported for Mn antimonate with a similar starting composition and under comparable conditions.[28] Contrasting this behaviour, the activity of [Mn+Sb]O_y synthesised herein with 1 : 1 and 1 : 2 ratios was highly stable. Between these two types of materials, the Sb-rich one was found to be less active, exhibiting η_{IR} for 10 mA cm^{-2} of *ca* 0.70 V. The best-performing [Mn+Sb]O_y electrocatalysts with the initial equimolar Mn : Sb ratio stably maintain the OER current density of 10 mA cm^{-2} for at least 24 hours under ambient conditions at a highly reproducible overpotential of 0.677 ± 0.008 V (**Figures** 1b and **S13**).

Combination of ruthenium with the antimonate matrix produced catalysts that exhibit a stable cyclic voltammetric response typical of a robust and highly active OER catalyst up to 2.03 V *vs.* RHE, in contrast to unstable RuO_x (Figures 1a, S3e and S6e). Moreover, galvanostatic tests at 10 mA cm^{-2} improved the performance of the [Ru+Sb]O_y materials by *ca* 0.04 V over the initial *ca* 10-12 h of experiments, eventuating in a reproducible stabilised IR_u-corrected overpotential of η_{IR} = 0.39 ± 0.03 V (**Figures** 1b and **S14**).

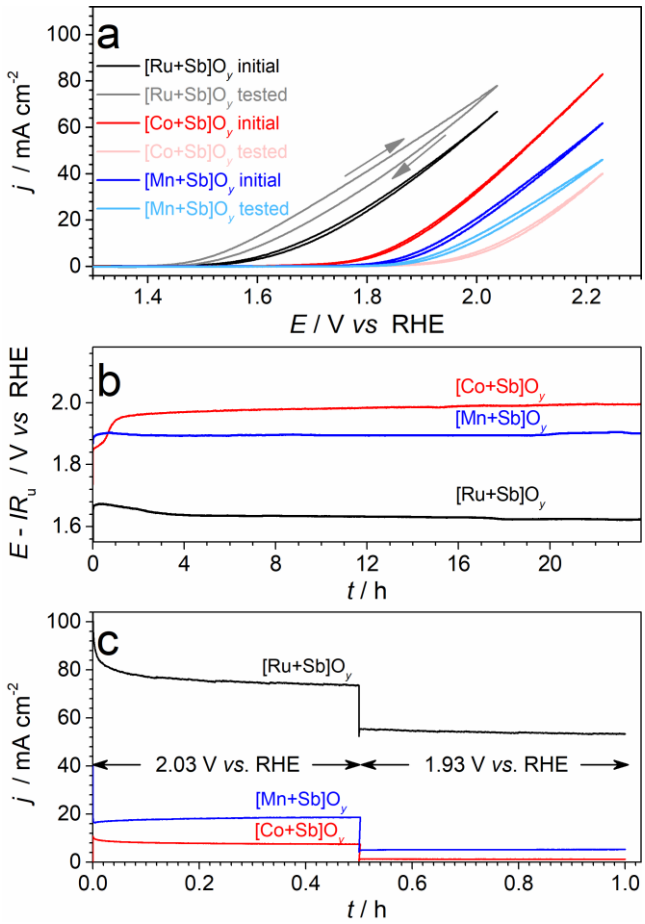

Figure 1. Electrochemical characterisation of [Co+Sb]O_y (*red*), [Mn+Sb]O_y (*blue*) and [Ru+Sb]O_y (*black*) in stirred 0.5 M H_2SO_4 at 24 ± 2 °C: (a) cyclic voltammetry (scan rate 0.020 V s^{-1}; third scans; no IR_u correction applied) recorded before (vivid traces) and after (pale traces) tests shown in panels b and c (arrows exemplify the direction of the voltammetric sweeps, which was qualitatively the same for all catalysts); (b) IR_u-corrected chronopotentiograms (current density 10 mA $cm^{-2}_{geom.}$); and (c) subsequently recorded chronoamperograms (at a non-IR_u-corrected potentials of 2.03 and 1.93 V vs. RHE).

Overall, the analysis of the initial catalytic performance and 25 h stability at ambient temperature of the metal-antimony oxides revealed a synergistic effect of the combination of a catalytically active metal and acid-stable Sb for the [Mn+Sb]O_y system, where a significant improvement in the activity was achieved. The key advantage of combining Co and Ru with the SbO_x matrix is in the substantial improvements in the stability, which is a highly favourable outcome given that the instability of the OER anode catalysts is among the most technologically pressing problems of the PEM water electrolysers.[32]

2.2 Characterisation of the mixed metal-oxide catalysts

To enable deeper understanding of the observed trends in the electrocatalytic performance of the investigated metal-antimony oxides, physical characterisation of the key materials was undertaken using the state-of-the-art techniques.

2.2.1 Corrosion during operation

SEM images of the [M+Sb]O_y electrodes taken before and after the OER tests revealed that the catalyst coatings underwent partial erosion due to the loss of material during the OER (**Figure S15**). The level of this loss was quantified for the key catalysts by ICP-OES (**Table 1**), while the changes in the catalyst surface compositions were estimated by X-ray photoelectron spectroscopy (XPS).

After 24 h galvanostatic followed by 1 h potentiostatic tests at ambient temperature, the levels of corrosion of metals and antimony from [Co+Sb]O_y and [Mn+Sb]O_y into the electrolyte solutions were comparable (Table 1), notwithstanding a very distinct electrocatalytic behaviour (Figure 1). XPS showed that concentrations of the metals at the surface of tested [Co+Sb]O_y and [Mn+Sb]O_y were also similar (**Table 2**). At the same time, voltammetric analysis, which provides the only reliable means of probing the catalytically active species, indicated that [Mn+Sb]O_y still exhibit detectable peaks associated with Mn redox transformations after the OER (Figure S8b), while operated [Co+Sb]O_y present a featureless response (Figure S8a). These observations might reflect the differences in the quasi-stabilised concentrations of the catalytically active metals in the top-most layers of the Co-Sb and Mn-Sb oxide systems. While the [Co+Sb]O_y surface loses a very significant part of its cobalt, [Mn+Sb]O_y is likely to maintain a higher amount of manganese available for the OER catalysis.

Table 2. Relative surface concentrations of metals for catalysts[a)] before and after OER tests in stirred 0.5 M H_2SO_4.

Catalyst	As prepared	Tested at	
		24 ± 2 °C [b)]	80 °C [c)]
[Mn+Sb]O_y	23 ± 1	12 ± 2	n.a.
[Co+Sb]O_y	34 ± 2	9 ± 4	n.a.
[Ru+Sb]O_y	9 ± 5	n.a.	44 ± 5

[a)] at.% with respect to total metal + antimony amount quantified by XPS; data are presented as a mean ± one standard deviation for several measurements. [b)] 10 mA cm^{-2} for 24 h and 2.03 and 1.93 V *vs.* RHE for 0.5 h at each potential. [c)] 10 mA cm^{-2} for 10 h.

The lowest level of metal corrosion was observed for [Ru+Sb]O_y where the amount of lost ruthenium was not more than 1 at.% at ambient temperature, but the amount of antimony released into the electrolyte solution was significant (Table 1). This was accompanied by a slight increase in the pre-catalytic voltammetric currents (Figure S9e). Most critically, long-term tests of [Ru+Sb]O_y at elevated temperature of 80 °C (*vide infra*) caused only slightly higher level of corrosion (Table 1), while XPS consistently demonstrated that the surface Ru : Sb ratio increased up to *ca* 1 : 1 (Table 2). Thus, [Ru+Sb]O_y suffers a favourable corrosion of antimony that improves the electrocatalytic activity of the material towards the OER (Figures 1b and 2a) through an enrichment of the surface layer in catalytically active ruthenium.

When considered together, the observed levels of corrosion (Tables 1 and 2) and stable electrocatalytic performance of the manganese-, cobalt- and ruthenium-antimony oxides (except for the initial drop in the [Co+Sb]O_y performance) (Figure 1) suggest that a quasi-equilibrium between the solid oxides and dissolved forms of Mn/Co/Ru and Sb is established in the system. Such an equilibrium between dissolution/redeposition of metal oxides is likely to sustain the observed stable electrocatalytic operation. In other words, the examined OER catalysts most probably operate in a self-healing mode,[20a, 20b, 33] with the Sb oxide matrix acting to facilitate the redeposition and suppress the dissolution of the active component.

2.2.2 Structural features

The structural features and the oxidation states of metals and antimony in the key [Co+Sb]O_y, [Mn+Sb]O_y and [Ru+Sb]O_y samples were probed by XAS (**Figure 2**), XPS (**Figures S16-S18**) and XRD (**Figure 3**). The ruthenium-antimony system was additionally investigated by TEM (**Figure 4**).

Fitting of the Sb 3d + O 1s spectra and comparisons to the literature[34] confirmed that antimony adopts a dominant oxidation state 5+ in all catalysts after the OER tests, as well as in most of the untreated samples (Figure S16). The Sb K-edge XANES recorded for Mn-, Co- and Ru-Sb mixed oxides reproduced well the data reported elsewhere for manganese antimonates,[28] and are again consistent with the 5+ state (**Figures** 2a and **S19**). A slight shift to higher energy was noted in the Sb K-edge after the OER tests (Figure S19). Sb K-edge EXAFS of the investigated metal-antimony oxides are similar to each other and to Sb_2O_5 in that none of the datasets exhibit any notable second coordination sphere peaks in the Fourier Transform (FT) of EXAFS beyond the first coordination sphere apparent distances (*R*') of 2 Å (**Figures** 2a and **S20**). This would be consistent with Sb being present as a part of a highly-disordered phase or might be the consequence of how the distances in the structure cancel each other out (**Figure S20 and Table S1**).

The shape and position of the Mn $2p_{5/2}$ peaks for fresh [Mn+Sb]O_y are similar to those for the oxide/oxyhydroxide Mn^{3+} compounds,[35] and show only a slight shift towards higher binding energies after tests (Figure S17a). Comparisons of the Mn K-edge XANES data for [Mn+Sb]O_y to that for the MnO, Mn_2O_3 and MnO_2 standards suggest that the oxidation state of the metal in the bulk of the as-prepared material is between 2+ and 3+, while Mn^{3+} becomes a dominant component after the OER tests (**Figures** 2b and **S21**).

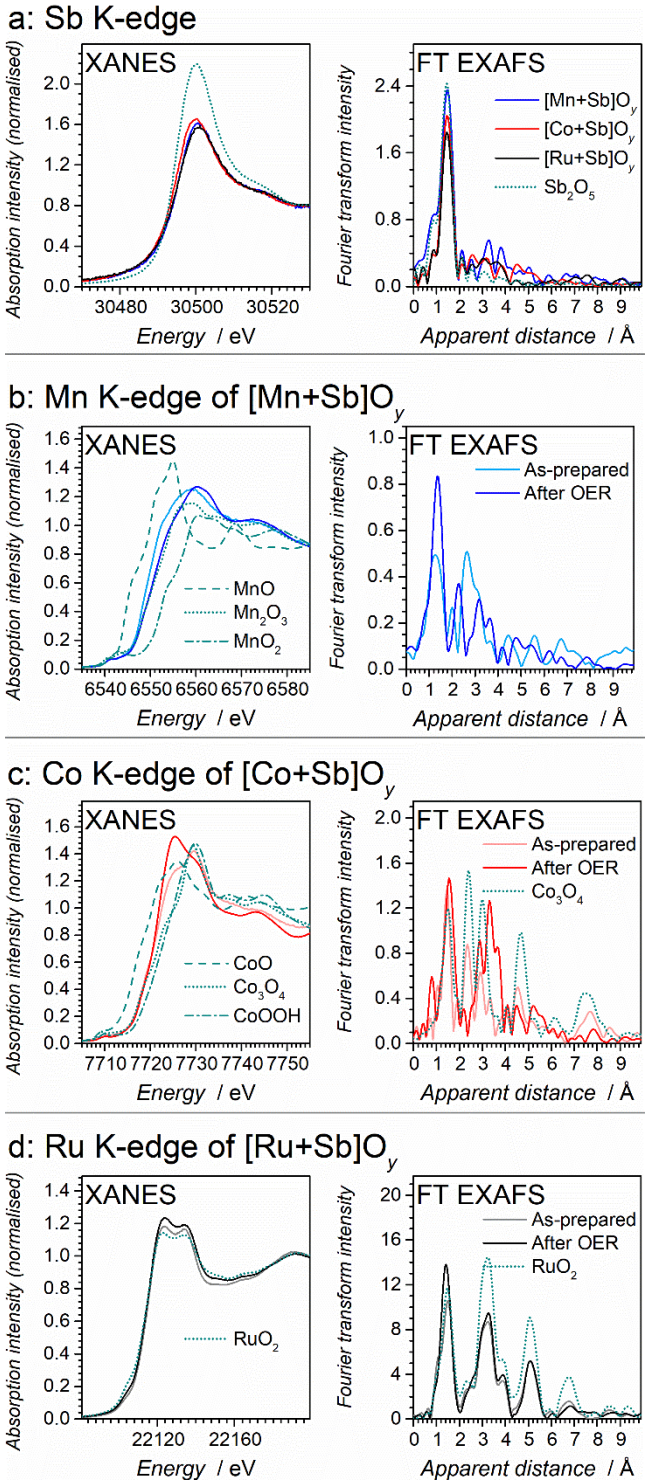

Figure 2. XAS data at (a) Sb, (b) Mn, (c) Co and (d) Ru K-edges obtained for [Mn+Sb]O$_y$ (*blue*), [Co+Sb]O$_y$ (*red*) and [Ru+Sb]O$_y$ (*black*) before (*pale solid traces*) and after (*vivid solid traces*) electrocatalytic tests in stirred 0.5 M H_2SO_4 compared to the defined reference materials (*dashed* and *dotted teal* traces). (e-h) Fourier Transform of EXAFS at (e) Sb, (f) Mn, (g) Co and (h) Ru K-edges. [Mn+Sb]O$_y$ and [Co+Sb]O$_y$ were tested for 24 h at 10 mA cm^{-2} and then for 1 h at 2.03 and 1.93 V *vs.* RHE at ambient temperature; [Ru+Sb]O$_y$ was tested for 12 h at 10 mA cm^{-2} at 80 °C.

The Co K-edge XANES of as-prepared [Co+Sb]O_y is consistent with an oxidation state between 2+ and 3+, or a material like Co_3O_4 (Figure 2c). The Co K pre-edge intensity decreases after the OER test, which would be consistent with the loss of the Co_3O_4 phase with a tetrahedral Co^{2+} site (**Figure S22a-b**), which is also supported by changes in the XANES profile (Figure 2c). The major Co oxidation state on the surface can be also ascribed to 3+ based on the XPS analysis (Figure S17b) and comparisons to the literature.[35]

Thus, both XPS and XANES indicate that the dominating oxidation states of manganese and cobalt in as-prepared metal-antimony mixed oxides are between 2+ and 3+. Although Mn and Co at the catalytic surfaces likely adopt higher oxidation states during the OER, those cannot be detected by *ex situ* analysis due to their very high oxidative reactivity and immediate conversion into states that are thermodynamically favourable under ambient environment.[36]

X-ray diffractograms of [Co+Sb]O_y and [Mn+Sb]O_y exhibited a set of peaks typical of a tetragonal trirutile phase with major 110, 013 and 123 reflections at *ca* 27, 35 and 53°, respectively (Figure 3a-b). Qualitatively similar XRD patterns were obtained for the mixed nickel-antimony and iron-antimony samples (**Figure S23**). These data agree with the recent studies,[23a, 28, 30] and formally suggest that the metal-antimony phase in the investigated materials is structurally similar to $CoSb_2O_6$. It is also worth noting that the mean crystallite sizes for the individual metal oxides phases detected by XRD were notably higher than those for the antimonate phase (Figure 3a-b), suggesting that the former are present as larger agglomerates as compared to the latter and therefore make significantly lower contribution to the electrocatalytically active surface area.

Well-defined FT EXAFS beyond the first coordination sphere were observed at the metal K-edges for [Co+Sb]O_y and [Mn+Sb]O_y (Figure 2b-c). This indicates that the metals do not simply dope the antimony oxide lattice, as was observed previously for the conceptually similar Co-Fe-Pb oxide OER catalyst,[20a] and more complicated structural scenarios apply. To describe the metal-antimony phases, EXAFS simulations based on the crystal structure of $MnSb_2O_6$[37] and that of $CoSb_2O_6$[38] were undertaken.

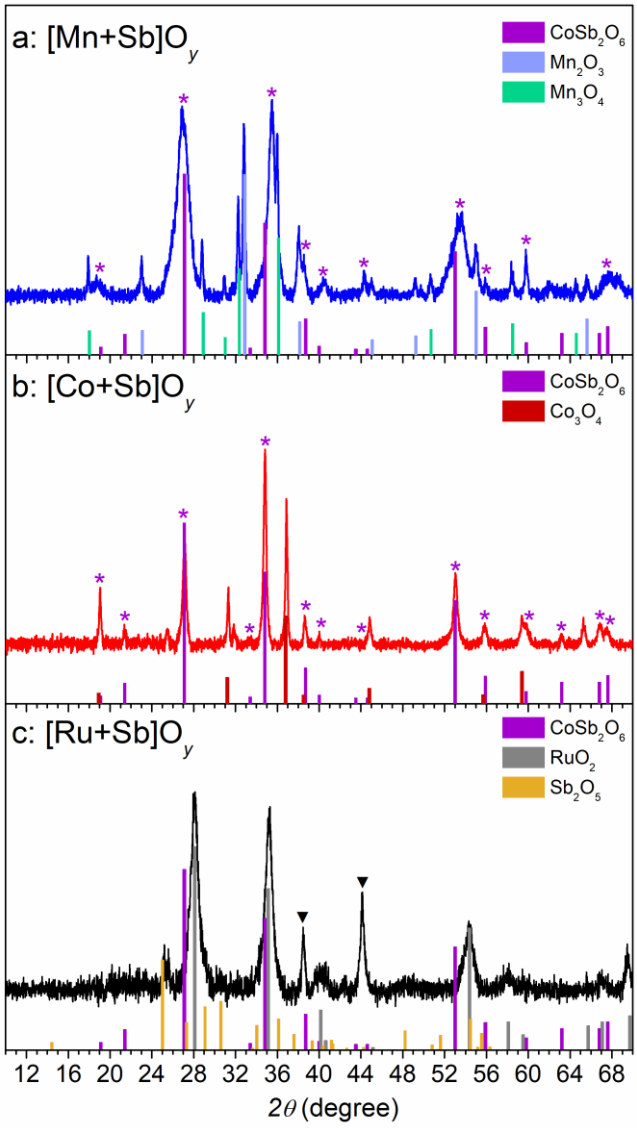

Figure 3. X-ray diffractograms of as-synthesised (a) [Mn+Sb]O_y, (b) [Co+Sb]O_y and (c) [Ru+Sb]O_y. Vertical lines show tabulated positions and relative intensities for (a-c) $CoSb_2O_6$ ICSD-108964, (a) Mn_2O_3 ICDD-00-041-1442 and Mn_3O_4 ICDD-01-075-1560, (b), Co_3O_4 ICSD-36256, (c) RuO_2 ICSD-731469 and Sb_2O_5 PDF-01-071-0256. Mean crystallite sizes calculated using Scherrer equation were: (a) $d_{XRD}(MnSb_2O_6) \approx 7$ nm, $d_{XRD}(Mn_2O_3) \approx 35$ nm, $d_{XRD}(Mn_3O_4) \approx 41$ nm; (b) $d_{XRD}(CoSb_2O_6) \approx 24$ nm; $d_{XRD}(Co_3O_4) \approx 43$ nm; (c) $d_{XRD}(RuO_2) \approx 10$ nm. Asterisks indicate diffraction peaks attributed to the antimonate phase. Triangles indicate peaks which assignment is not straightforward.

As expected from XRD (Figure 3a), $MnSb_2O_6$ alone could not describe the Mn K-edge EXAFS for as-prepared [Mn+Sb]O_y (**Table S2**) due to the presence of a manganese oxide compound, most likely Mn_2O_3, which produces a peak at *ca* 2.5-2.6 Å in FT EXAFS (Figures 2b and S21f). After the OER, the intensity of the Mn_2O_3 features in EXAFS are suppressed (Figures 2b and S21c, Table S2), which indicates partial loss of Mn_2O_3 and corroborates the corrosion data (Table 1). Given that this loss does

not induce any notable deterioration in the catalytic activity (Figure 1b), we conclude that individual Mn oxides do not make a significant contribution to the OER performance of [Mn+Sb]O_y.

XAS data recorded at the Co K-edge for [Co+Sb]O_y confirmed the XRD observations of the presence of Co_3O_4 in the as-prepared material, which vanished after the OER tests (Figure 2c and S22c,e). The XAS data of the tested catalyst are well fit with the simulations based on the $CoSb_2O_6$ structure[38] (Figure S22c,f and **Table S3**). On this basis, we interpret the initial rapid drop in the performance of [Co+Sb]O_y (Figure 1b) by the dissolution of the catalytically more active Co_3O_4 phase from the material surface, while the quasi-stabilised performance achieved after *ca* 20 h is ascribed to the true catalytic activity of cobalt antimonate.

The most challenging to interpret set of physical characterisation data among examined systems was obtained for the top-performing [Ru+Sb]O_y catalyst. Analysis of the Ru 3d XP spectra is complicated by a direct overlap with C 1s signals, but it was still possible to conclude that the initial mixed Ru^{3+} + Ru^{4+} state of the surface undergoes oxidation during the OER to become dominated by Ru^{4+} (Figure S17c and S18c).[39] In turn, Ru K-edge XANES recorded for fresh and tested [Ru+Sb]O_y were in a perfect agreement with the Ru^{4+} state, closely resembling the spectra of RuO_2 (Figure 2d).

Interpretation of the XRD data for [Ru+Sb]O_y was not straightforward as the diffraction pattern of rutile RuO_2 is similar to that of the anticipated trirutile antimonate phase. Nevertheless, the major set of broad diffraction peaks at 28, 35, 40, 54 and 69.5° matches well the positions and relative intensities of the tabulated pattern of ruthenium (IV) oxide (*grey bars* in Figure 3c). This interpretation suggests that the Sb component(s) give rise to a set of broad low-intensity signals at *ca* 25, 30.5 and 48° that can be attributed to highly disordered Sb_2O_5, along with two peaks at *ca* 38.5 and 44° (marked with triangles Figure 3c). One might suggest that these two reflections can be attributed to an antimonate phase which other diffraction peaks are presumably merged with the signals of RuO_2. However, analysis of the highly resolved up to R' = 8 Å Ru K-edge EXAFS collected for [Ru+Sb]O_y does not support this hypothesis (**Figures** 2d and **S24**). Fitting of these data with simulations based on a $RuSb_2O_6$-type lattice did not produce any satisfactory level of agreement

(Figure S24 and **Table S4**). Clearly resolved FT EXAFS peaks at high *R*' of 3.1, 3.9, 5.1, 6.8 Å present in the catalyst before and after the OER tests are associated with groups of Ru-Ru distances at 5.0, 6.8 and 7.2 Å, and cannot be explained by the $RuSb_2O_6$ phase. In fact, the EXAFS and XANES of $[Ru+Sb]O_y$ are almost perfectly consistent with the RuO_2 structure, although with a slightly increased level of disorder (Figures 2d and S24, Table S4), which corroborates the major XRD signals (Figure 3c).

Taken together, XAS and XRD suggest that the ruthenium structure in $[Ru+Sb]O_y$ is very close to the RuO_2 lattice, which opens a question on the origin of the significantly improved electrocatalytic performance of the mixed oxide system as opposed to RuO_2 (Figure 1 and S4a). To shed light on this, detailed TEM investigations with elemental mapping were undertaken.

At low to moderate magnification, STEM-EDS analysis of $[Ru+Sb]O_y$ showed ruthenium and antimony to be intimately mixed, both before and after the OER tests (**Figures** 4a-b and **S25**). Conventional TEM imaging demonstrated that the catalyst represents a very fine assembly of nanocrystals, typically less than 10 nm in size, embedded into another material that appears significantly more structurally disordered (**Figures** 4c-d and **S26**). Higher magnification images revealed clear lattice fringes of *ca* 3 Å for the crystalline nanoparticles, which can be attributed to RuO_2 with a relatively high degree of crystalline order (Figure 4c-d).

This is also illustrated in the selected area electron diffraction pattern, which can be indexed as essentially pure RuO_2 (Figure 4e) notwithstanding it was recorded from a large fragment containing both ruthenium and antimony. The material closely neighbouring RuO_2 nanocrystals exhibited larger lattice fringes of *ca* 4-5 Å (Figure 4d), which cannot be ascribed to ruthenium oxide and therefore are attributed to antimony oxides. STEM-EDS mapping of this area confirmed the partial segregation of ruthenium and antimony at the nanoscale (Figure 4f), but we emphasise that the two elements were still found to be mixed very finely, even when analysed at up to 1.3M× magnification (**Figures** 4f and **S27**).

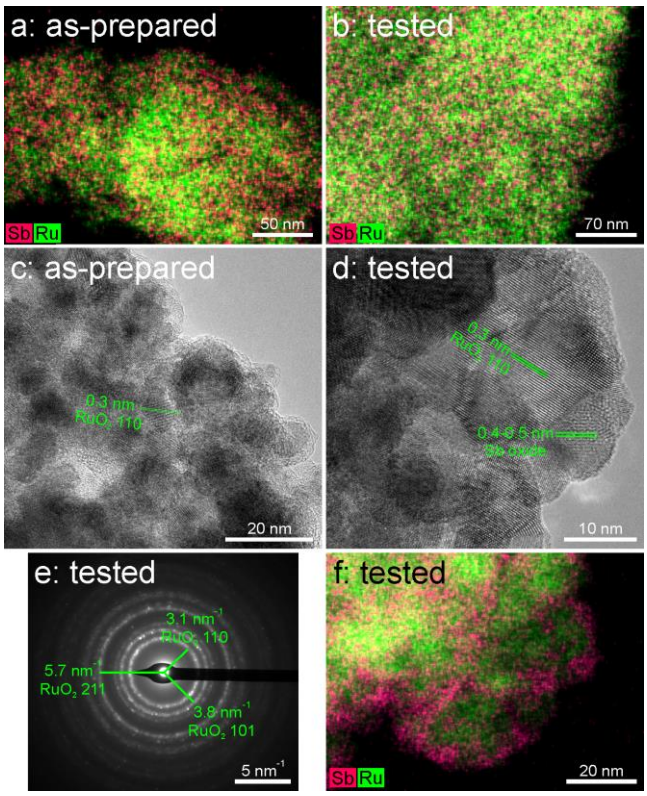

Figure 4. TEM and STEM-EDS characterisation of [Ru+Sb]O_y before and after OER tests in stirred 0.5 M H_2SO_4 at 10 mA cm^{-2} for 24 h at 80 °C: (a-b) medium magnification STEM-EDS mapping of the (a) as-prepared and (b) tested catalyst; (c-d) TEM micrographs of the (c) as-prepared and (d) tested catalyst; (e) selected area electron diffraction taken from a region containing large amounts of both Ru and Sb for the tested catalyst. (f) STEM-EDS mapping analysis of the extended area of the tested catalyst around the region shown in panel d.

Other antimony rich areas were generally devoid of clear lattice fringes (Figure 4c-d), and although this does not definitely rule out crystallinity, it tends to support a hypothesis that Sb oxides in [Ru+Sb]O_y exhibit a very high level of disorder. We also note that the Sb phase appears to coat the edges and interstices of the RuO_2 nanocrystals in the catalysts after the OER test (Figure 4f), suggesting that antimony has been lost from a previously predominating Sb-based coating of Ru oxide particles rather than a simple aggregation of two phases. This supports the corrosion data (Table 1).

Overall, the physical characterisation data reveal several fundamental differences in the investigated catalysts. As-prepared [Mn+Sb]O_y and [Co+Sb]O_y contain a mixture of individual metal oxides, which majorly dissolve during the OER tests, with a metal antimonate oxide phase. The latter is most likely $CoSb_2O_6$ in [Co+Sb]O_y, while the structure of the manganese-antimony oxide exhibits some

distinctions from the published features of the antimonate phase and a significant level of disorder. At the same time, no evidence for the formation of a ruthenium antimonate was obtained. Instead, the [Ru+Sb]O_y catalyst contains highly-dispersed RuO_2 crystallites embedded into and decorated with disordered antimony oxides. One might hypothesise that an interaction and intermixing between ruthenium and antimony oxides might still occur, but at the topmost surface layers of RuO_2, especially at the abundant intergrain boundaries visualised by TEM (Figure 4c-d), rather than in the bulk phase. To assess this possibility and further assist in establishing a plausible explanation of the improved electrocatalytic performance of [Ru+Sb]O_y, theoretical analysis of the metal-antimonate systems was undertaken.

2.3 Theoretical insights into the improved stability of the Co-Sb and Ru-Sb oxides

Experimental evidence on the stabilisation against corrosion of the oxides of transition metals like Co, Mn, Ni and Ru, through their combination with the oxides that are thermodynamically stable under the OER conditions exists,[7, 16-23] including the new results reported in the present work. However, there is a lack of the understanding behind this stabilising effect, which we aimed to address through the theoretical analysis of two systems of interest herein – Co-Sb and Ru-Sb mixed oxides. Extending the analysis to the Mn-Sb combination could not be realised due to a well-documented complex ground state magnetic structure of Mn_2O_3, which exhibits noncollinear magnetic ordering and introduces significant uncertainties to the modelling of the electronic structure.[40]

Assessment of the electrochemical and structural stability was undertaken through the computation of cohesive energies of the materials of interest and also differences in the dissolution potentials (ΔE_d)[41] for the Ru-Sb system. Both approaches have been previously validated through comparisons of the theoretical predictions and experimental electrochemical stability data for a range of systems, in particular metal oxides.[42]

For the Co-Sb combination, the simulated compositional phase diagram (**Figure 5a**) indicates a broad chemical potentials space that favours the formation of $CoSb_2O_6$ (structure shown in **Figure S28**) as

opposed to individual oxides. Experimental data suggest that this phase dominates the [Co+Sb]O_y catalyst under the OER conditions and was therefore used for further theoretical analysis. As a point of reference in the calculations, Co_3O_4 – the dominating phase of the CoO_x control – was considered. Cohesive energies for Co_3O_4 and $CoSb_2O_6$ were simulated as -12.8 eV and -15.4 eV per formula unit, respectively, which indicates improved overall structural and electrochemical stability[43] of the antimonate as compared to the monometallic oxide. The improvement in cohesive energies is likely to be partially associated with the higher bond energy for Sb-O (434 kJ mol^{-1}) as compared to Co-O (397 kJ mol^{-1}),[44] although one might note that this difference does not appear sufficient to explain the calculated cohesive energies. Therefore, we hypothesised if the presence of Sb in the structure might strengthen the Co-O bond through changes in the electronic structure.

The above supposition was assessed through the analysis of the atom/orbital projected partial density of states (PDOS), calculated bond lengths and Bader charges. The PDOS for Co_3O_4 demonstrates a reasonable hybridisation of the oxygen p-orbitals with d-orbitals of cobalt in tetrahedral sites but not in octahedral ones; this is in contrast to $CoSb_2O_6$ where only one type of Co sites is present and is strongly hybridised with O 2p (**Figure S29a-b**). It is also noted that the latter interact much stronger with Co 3d orbitals rather than with Sb 5p.

Since the electrocorrosion of materials is an interfacial phenomenon, the above findings were also corroborated by the analysis of the characteristic catalyst surfaces – (110) oriented facet for $CoSb_2O_6$ and (110)-A terminated surface for Co_3O_4[45] (Figure S28c-d). Comparisons of the PDOS of bulk and (110) surfaces suggest that the slab geometry produces surface states just above the valence band due to the undercoordinated Co^{3+}, Co^{2+} and O^{2-} ions, which renders these surfaces metallic. Similar to the bulk, 2p orbitals of the surface O in $CoSb_2O_6$ interact stronger with Co 3d as compared to Sb 5p orbitals. Enhanced O-p – Co-d interaction in $CoSb_2O_6$ is additionally verified by the calculated PDOS of sub d-orbitals of Co^{2+} in Co_3O_4 and $CoSb_2O_6$ (**Figure S30**).

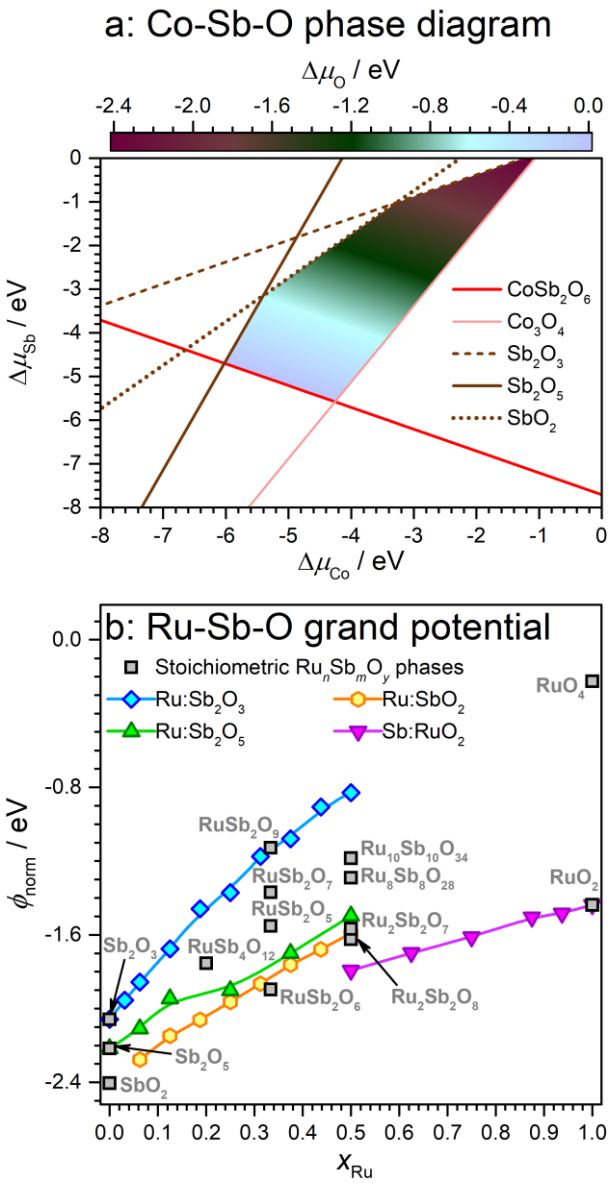

Figure 5. (a) Simulated compositional phase diagram of $CoSb_2O_6$ against individual oxides. Shaded area corresponds to the stable region of $CoSb_2O_6$, where the colour scale shows the allowed chemical potentials for oxygen; coloured lines and the corresponding spaces opposite to the shaded region present the stable regions of the identified individual oxides. (b) Normalised oxygen grand potential (ϕ_{norm}) *vs*. ruthenium atomic fraction, $x_{Ru} = n/(n + m)$, calculated for $[Ru_n+Sb_m]O_y$ at $T = 600$ °C and 0.21 atm O_2 partial pressure. Sb:RuO_2 – Sb-doped RuO_2; Ru:SbO_2, Ru:Sb_2O_3 and Ru:Sb_2O_5 – Ru-doped antimony oxides. Calculated data are shown as symbols; lines are guides to an eye.

The features of the PDOS discussed above can be expected to make the overall cohesive energy of $CoSb_2O_6$ more negative than that of Co_3O_4 and hence enhance the driving force required for the electrocorrosion of cobalt. Furthermore, the simulated Co-O and Sb-O bond lengths in $CoSb_2O_6$ were lower and higher than the corresponding expected values based on the combined ionic radii, respectively (2.08 Å calculated *vs.* 2.105 Å expected for high spin Co-O; 2.02 Å calculated *vs.* 1.98

Å expected for Sb-O). This internal compressive strain of the Co-O bonds can be associated with the higher electronegativity of Sb as compared to Co. Calculated Bader charges on Co^{2+} in Co_3O_4 and $CoSb_2O_6$ were +1.31*e* and +1.36*e*, respectively, which further supports the stronger Co-O bond in the antimonate as compared to the individual metal oxide.

Next, the ruthenium-antimony system was analysed following a similar approach. As discussed above, no robust experimental evidence for the formation of a stabile ruthenium-antimony oxide phase was obtained. In line with these experimental observations, total energies calculated by DFT simulations indicated that hypothesised $RuSb_2O_6$ phase is unstable with respect to the individual oxides (**Table S5**). This prompted us to undertake a simulation of a grand potential phase diagram of the Ru-Sb system (Figure 5b), which enables prediction of the thermodynamically stable compositions that can be formed under relevant synthesis conditions,[46] *i.e.* at $T = 600$°C and 0.2 atm O_2 partial pressure in the present work.

Oxygen grand potentials were calculated for various $[Ru_n+Sb_m]O_y$ structures and compositions as a function of the metal atomic fraction, $x_{Ru} = n/(n + m)$. In addition to a broad range of stoichiometric compounds, substitutional doping of Sb into RuO_2 (Sb:RuO_2) and Ru in antimony oxides was considered. Among these different possibilities, the lowest ϕ_{norm} at $x_{Ru} = 0.5$, *i.e.* the highest stability under the conditions employed during the synthesis of $[Ru+Sb]O_y$, was calculated for the ruthenium(IV) oxide doped with antimony. In fact, Sb:RuO_2 are theoretically predicted to be more stable than the parent metal oxide within the x_{Ru} range examined (Figure 5b). At the same time, the experimental XAS data provide a compelling evidence for the dominant state of ruthenium in $[Ru+Sb]O_y$ being very similar to that in RuO_2 (*vide supra*). On this basis, further analysis focused on RuO_2 at low levels of Sb doping.

Differences in the electronic properties of the RuO_2 reference and Sb:RuO_2 were investigated based on the computations with a 2×2×2 supercell of tetragonal 6-atom RuO_2 unit cell containing 16 Ru and 32 O atoms. First, through the examination of the calculated spin polarised total density of states, we note that Sb substitution into RuO_2 maintains its metallic character and even further improves the

electrical conductivity as concluded from the shift of the conduction band (**Figure S31**), which is a positive finding from the perspective of the electrocatalytic activity. Further, and most importantly, improved stability of Ru^{4+} within the Sb:RuO_2 materials was confirmed by the positive difference in the dissolution potential[41] ΔE_d = 0.08 V and by the negative increase in the cohesive energies when compared to undoped RuO_2. Specifically, the cohesive energy changes from -3.28 (RuO_2) to -3.51 ($Sb_{0.0625}$:$Ru_{0.9375}O_2$) and -3.62 eV per unit formula ($Ru_{0.813}Sb_{0.187}O_2$). This favourable change is again explained by the enhanced strength of the Ru-O bond, which is indicated by the stronger overlap of O 2p and Ru 3d orbitals in the PDOS (**Figure S32**) as well as by the higher Bader charge on ruthenium in $Sb_{0.0625}$:$Ru_{0.9375}O_2$ (+1.76e) as compared to RuO_2 (+1.70e). Enhanced charge donation from ruthenium to neighbouring oxygen atoms is also supported by the differences in the partial density of states of Ru 4d sub-orbitals (**Figure S33**).

In summary, the computational analysis suggests that the improvement in the stability of Ru and Co oxides upon combination with Sb oxide is majorly stemming from the electronic effects of antimony that strengthen the metal-oxygen bonds. Aggregate of the experimental and computational data for the Ru-Sb system suggests that, although the well-defined ruthenium antimonate phase is unlikely to be formed, doping of ruthenium(IV) oxide with antimony is possible. Taking into account the experimental data indicating the formation of the slightly distorted RuO_2 phase (Figures 2d, 3c and 4) and the very significant level of corrosion of antimony but not of ruthenium during the OER tests of [Ru+Sb]O_y (Tables 1 and 2), we hypothesise that Sb doping might be majorly confined to the surface of the RuO_2 crystallites. The formation of this protective layer is likely to be sufficient to provide the enhanced stability of the material against the electrocorrosion highlighted above (Figure 1) and as even more strongly emphasised through the durability tests at elevated temperature that are discussed below.

2.4 Longer-term operation at elevated temperature

A final set of tests was undertaken to assess the ability of the two most promising catalysts investigated herein, *viz.* [Mn+Sb]O_y and [Ru+Sb]O_y, to operate for extended periods of time and at elevated temperatures. Voltammetric analysis confirmed the expected positive effect of increasing the temperature on the kinetics of the OER catalysed by both Mn- and Ru-based materials (**Figure 6a-b**). The apparent activation energy of the OER at an *IR*-corrected overpotential of 0.6 V approximated from the backward potentiodynamic scans for [Mn+Sb]O_y is *ca* 20 ± 10 kJ mol^{-1} (**Figure S34**). This is notably lower than values reported for other OER catalysts operating at low pH,[47] and probably reflects the increasing instability of this material at elevated temperatures as discussed below.

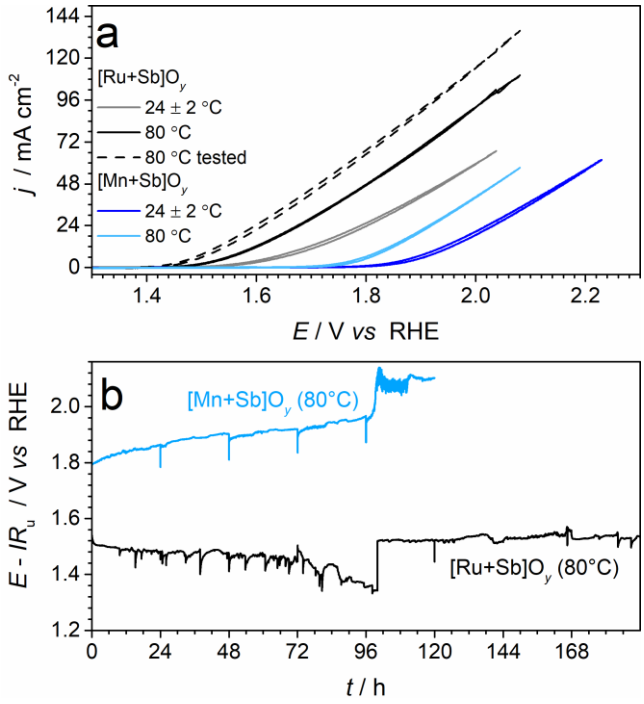

Figure 6. Performance of the [Ru+Sb]O_y (*black*) and [Mn+Sb]O_y (*blue*) catalysts during the OER in stirred 0.5 M H_2SO_4 at 80 °C: (a) cyclic voltammetry (scan rate 0.02 V s^{-1}; not IR_u-corrected; third scans) before (*vivid traces*) and after (*pale traces*) long-term tests shown in panel b (dashed curves show data collected at 24 ± 2 °C), and (b) IR_u-corrected chronopotentiograms (10 mA cm$^{-2}_{geom.}$).

While no significant deterioration of the [Mn+Sb]O_y performance was observed in the voltammetric regime (**Figure S35a**), short-term 24 h galvanostatic tests revealed that this catalyst suffers detectable losses in activity at 60 °C (Figure S35b-c). During these experiments, the overpotential required to maintain the OER rate of 10 mA cm^{-2} increased almost linearly, meaning an exponential decrease in

the activity of the catalyst, at an average rate of *ca* 0.001-0.002 V h^{-1}. When longer-term testing was undertaken at 80 °C, degradation at essentially the same rate was observed over the initial *ca* 100 h of measurements (Figure 6b). Afterwards, an abrupt loss of the performance, reflected by an increase of the potential to *ca* 2.1 V *vs.* RHE occurred, which was then maintained for at least another 24 h. The latter observation suggests that the change in the OER activity observed in these experiments is unlikely to be associated with the degradation of the FTO support, which would result in a complete loss of any ability of the electrode to sustain water electrooxidation due to the disruption of the electrical contact. On the basis of these new data (Figures 1b and 6b; Figure S35b), we conclude that manganese antimonate is a promising non-noble-metal-based water oxidation catalyst capable of a reasonably stable operation in acidic electrolyte solutions, but it is unlikely to be suitable for applications at 60 °C and higher temperatures.

The behaviour of [Ru+Sb]O_y at 80 °C was remarkably different to that of [Mn+Sb]O_y (**Figures** 6a and **S36**). First, the ruthenium-based catalyst demonstrated a robust operation for 192 h of chronopotentiometry at 10 mA cm^{-2} and additional 1 h of chronoamperometry at 2.03 and 1.93 V *vs.* RHE (Figure 6b and S36b-c). Apart from the self-healing Co-Fe-Pb system,[20a] we are not aware of any other recently reported OER electrocatalyst capable of similarly stable operation under such comparably harsh conditions. Second, comparisons of the cyclic voltammetric data recorded before and after long-term tests reveal a notable improvement in the performance of the catalyst. This positive change was also observed in short-term ambient temperature tests (Figure 1a) and is likely to be associated with a significant increase of the amount of ruthenium on the surface due to the loss of the catalytically inactive SbO_x (Table 2) but not Ru (Table 1). The stabilised catalytic activity for the OER of an essentially flat [Ru+SbO_y] electrode at 80 °C and pH 0.3 corresponds to the reaction rate of 10 mA $cm^{-2}_{geom.}$ at an *IR*-corrected overpotential of 0.33-0.35 V (1.51-1.53 V *vs.* RHE).

To further emphasise the significance of the above results, we note that publications on low-pH water oxidation catalysts ubiquitously report chronopotentiometric profiles that demonstrate an increase in the potential with time, which might be small but persistent and essentially always present. The

[Ru+Sb]O_x material described herein contrasts this by *improving* in performance during tests and showing *no positive potential* change with respect to the initial value when tested at ambient (Figure 1b) and even at elevated (Figure 6b) temperatures. When evaluated in terms of the S-number metrics, *viz.* the amount of O_2 evolved per the amount of the catalytically active metal dissolved, [Ru+Sb]O_x is on par with the benchmark Ir-based catalysts and outperforms recently investigated Ru-based materials also tested as flat thin films at the same or comparable OER current densities at ambient temperature (*cf.* data in Table 1 to those reported in Refs.[5a, 48]). Particularly remarkable is the very high *S*-number for [Ru+Sb]O_x recorded herein at 80 °C. It is also noted that the *S*-number for the [Mn+Sb]O_x catalyst is of the same order of magnitude as that reported for the ruthenium pyrochlore catalysts elsewhere.[48]

3. Conclusions

The combination of transition metal and antimony oxides in a pursuit of the creation of robust and active catalysts for the electrooxidation of water under acidic conditions was found to produce very different outcomes depending on the chemical nature of the metal employed. While nickel and iron did not yield efficient catalytic systems, mixing Sb with cobalt, manganese and ruthenium resulted in materials with quite distinct structural features, but all demonstrating one very significant and critically important advantage with respect to the individual metal oxides – significantly improved operational stability. The origin of this positive effect can now be explained by the antimony-induced increase in the metal-oxygen bond strength, which substantially suppresses the electrooxidative dissolution, as revealed through the computational studies. The theoretical treatment implemented herein might be considered for future high-throughput screening studies for the identification of robust electrocatalysts for the OER.

Another set of key findings of the present work stems from the exhaustive durability tests of the materials at different temperatures. While demonstration of apparently stable operation of the oxygen evolution reaction catalysts at low pH and ambient temperature on a short timescale does not present

a very significant research challenge anymore, longer term operation at elevated temperatures of practical interest is still hard to achieve. Herein, the instability of the promising manganese-antimony oxide catalysts at 60-80 °C was revealed to indicate that this system needs to be further improved if it is intended to be designed for operation in PEM water electrolysers. Contrasting this behaviour, mixed ruthenium-antimony oxides were found to be stable in operation at 80 °C for at least one week, accompanied by negligible loss of the catalytically active metal into the solution. This corresponds to the very high *S*-number values well above 10^5. The lack of any recent reports on a similar performance during the electrooxidation of acidic water under comparably harsh conditions allows us to consider this result as outstanding and highly promising in the context of the development of the anode catalysts for PEM water electrolysers.

Finally, the aggregate of results presented herein suggests that there might be two different mechanisms for stabilising electrocatalytically active species like cobalt, manganese, or ruthenium oxides *via* the combination with an acid-stable "matrix" during water oxidation. The first is the formation of metal-matrix compounds either through doping or *via* transformation into new phases like antimonates. The second, less obvious and highlighted in detail herein for the ruthenium-antimony oxide system, is based on the intimate mixing of the discrete phases at the nanoscale. This mechanism might form a basis for a new promising strategy towards the design of electrocatalytic systems that exhibit outstanding stability while maintaining the high activity of the individual metal oxide.

Acknowledgements

Different parts of this work were undertaken at the XAS beamline of the Australian Synchrotron, Monash Centre for Electron Microscopy (partially funded through ARC LIEF project LE 110100223), Monash X-ray platform, Indian National Centre for Photovoltaic Research and Education (NCPRE), Sophisticated Analytical Instrument Facility (SAIF), Central Surface Analytical Facility of IIT Bombay, and spacetime2 cluster at IIT Bombay; the authors are highly grateful for being provided with access to these facilities and resources. The financial support of this work by the Australian Research Council (Centre of Excellence for Electromaterials Science CE140100012; Future Fellowship to ANS; Laureate Fellowship to DRM), the Australian Renewable Energy Agency ("Renewable Hydrogen for Export" project 2018/RND008 AS008), MNRE Government of India (NCPRE-Phase II, IIT Bombay to AA and AYella), Early Career Research Award, Science and Engineering Research Board, Government of India (ECR/2016/000550 to AYella), and IITB-Monash Academy (PhD scholarship to SL) is gratefully acknowledged. The authors also sincerely thank Dr T. Gengenbach (CSIRO, Australia) for guidance in the interpretation of the XPS data and Mr H. Takur (IIT Bombay) for assistance with the collection of some of the XRD data.

References

[1] a) T. Reier, H. N. Nong, D. Teschner, R. Schlögl, P. Strasser, *Adv. Energy Mater.* **2017**, *7*, 1601275; b) D. R. MacFarlane, J. Choi, B. H. R. Suryanto, R. Jalili, M. Chatti, L. M. Azofra, A. N. Simonov, *Adv. Mater.* **2019**, *32*, 1904804.

[2] *https://www.hydrogenics.com/2019/02/25/hydrogenics-to-deliver-worlds-largest-hydrogen-electrolysis-plant*.

[3] K. Ayers, N. Danilovic, R. Ouimet, M. Carmo, B. Pivovar, M. Bornstein, *Annual Review of Chemical and Biomolecular Engineering* **2019**, *10*, 219-239.

[4] J. Kibsgaard, I. Chorkendorff, *Nature Energy* **2019**, *4*, 430-433.

[5] a) S. Geiger, O. Kasian, M. Ledendecker, E. Pizzutilo, A. M. Mingers, W. T. Fu, O. Diaz-Morales, Z. Li, T. Oellers, L. Fruchter, A. Ludwig, K. J. J. Mayrhofer, M. T. M. Koper, S. Cherevko, *Nature Catal.* **2018**, *1*, 508-515; b) O. Kasian, J. P. Grote, S. Geiger, S. Cherevko, K. J. J. Mayrhofer, *Angewandte Chemie - International Edition* **2018**, *57*, 2488-2491; c) F. Claudel, L. Dubau, G. Berthomé, L. Sola-Hernandez, C. Beauger, L. Piccolo, F. Maillard, *ACS Catal.* **2019**, *9*, 4688-4698; d) O. Kasian, S. Geiger, T. Li, J. P. Grote, K. Schweinar, S. Zhang, C. Scheu, D. Raabe, S. Cherevko, B. Gault, K. J. J. Mayrhofer, *Energy and Environmental Science* **2019**, *12*, 3548-3555; e) V. A. Saveleva, L. Wang, O. Kasian, M. Batuk, J. Hadermann, J. J. Gallet, F. Bournel, N. Alonso-Vante, G. Ozouf, C. Beauger, K. J. J. Mayrhofer, S. Cherevko, A. S. Gago, K. A. Friedrich, S. Zafeiratos, E. R. Savinova, *ACS Catal.* **2020**, *10*, 2508-2516.

[6] G. Chen, J. Li, H. Lv, S. Wang, J. Zuo, L. Zhu, *Royal Society Open Science* **2019**, *6*.

[7] X. Li, D. Pletcher, F. C. Walsh, *Chem. Soc. Rev.* **2011**, *40*, 3879-3894.

[8] Z. Lei, T. Wang, B. Zhao, W. Cai, Y. Liu, S. Jiao, Q. Li, R. Cao, M. Liu, *Adv. Energy Mater.* **2020**, *10*, 1-18.

[9] a) S. A. Bonke, M. Wiechen, R. K. Hocking, X.-Y. Fang, D. W. Lupton, D. R. MacFarlane, L. Spiccia, *ChemSusChem* **2015**, *8*, 1394-1403; b) S. A. Bonke, A. M. Bond, L. Spiccia, A. N. Simonov, *J. Am. Chem. Soc.* **2016**, *138*, 16095-16104; c) G. Liu, S. K. Karuturi, A. N. Simonov, M. Fekete, H. Chen, N. Nasiri, N. H. Le, P. Reddy Narangari, M. Lysevych, T. R. Gengenbach, A. Lowe, H. H. Tan, C. Jagadish, L. Spiccia, A. Tricoli, *Adv. Energy Mater.* **2016**, *6*, 1-9; d) R. K. Hocking, R. Brimblecombe, L. Y. Chang, A. Singh, M. H. Cheah, C. Glover, W. H. Casey, L. Spiccia, *Nature Chemistry* **2011**, *3*, 461-466; e) R. Beltrán-Suito, V. Forstner, J. N. Hausmann, S. Mebs, J. Schmidt, I. Zaharieva, K. Laun, I. Zebger, H. Dau, P. W. Menezes, M. Driess, *Chemical Science* **2020**, *11*, 11834-11842; f) R. D. L. Smith, M. S. Prévot, R. D. Fagan, Z. Zhang, P. A. Sedach, M. K. J. Siu, S. Trudel, C. P. Berlinguette, *Science* **2013**, *340*, 60-63; g) M. Chatti, A. M. Glushenkov, T. Gengenbach, G. P. Knowles, T. C. Mendes, A. V. Ellis, L. Spiccia, R. K. Hocking, A. N. Simonov, *Sustainable Energy and Fuels* **2018**, *2*, 1561-1573; h) L. Trotochaud, S. L. Young, J. K. Ranney, S. W. Boettcher, *J. Am. Chem. Soc.* **2014**, *136*, 6744-6753.

[10] C. C. L. McCrory, S. Jung, I. M. Ferrer, S. M. Chatman, J. C. Peters, T. F. Jaramillo, *J. Am. Chem. Soc.* **2015**, *137*, 4347-4357.

[11] a) R. Frydendal, E. A. Paoli, I. Chorkendorff, J. Rossmeisl, I. E. L. Stephens, *Adv. Energy Mater.* **2015**, *5*, 1500991; b) J. S. Mondschein, J. F. Callejas, C. G. Read, J. Y. C. Chen, C. F. Holder, C. K. Badding, R. E. Schaak, *Chem. Mater.* **2017**, *29*, 950-957.

[12] B. S. Van Gosen, P. L. Verplanck, R. R. Seal Ii, K. R. Long, J. Gambogi *Rare-earth elements*; 1802O; Reston, VA, 2017; p 44. https://doi.org/10.3133/pp1802O.

[13] L. Bloxham, A. Cowley, L. Han, E. Shao, *JM* **2020**, *February*, 1-48.

[14] R. F. Schulte, *USGS* **2018**, *703*, 124-125.

[15] a) S. Song, H. Zhang, X. Ma, Z. Shao, R. T. Baker, B. Yi, *Int. J. Hydrogen Energy* **2008**, *33*, 4955-4961; b) S. Cherevko, S. Geiger, O. Kasian, N. Kulyk, J. P. Grote, A. Savan, B. R. Shrestha, S. Merzlikin, B. Breitbach, A. Ludwig, K. J. J. Mayrhofer, **2016**, *262*, 170-180; c)

O. Kasian, S. Geiger, P. Stock, G. Polymeros, B. Breitbach, A. Savan, A. Ludwig, S. Cherevko, K. J. J. Mayrhofer, *J. Electrochem. Soc.* **2016**, *163*, F3099-F3104.
[16] a) A. N. Nikoloski, M. J. Nicol, *Miner. Process. Extr. Metall. Rev.* **2010**, *31*, 30-57; b) S. Schmachtel, L. Murtomäki, J. Aromaa, M. Lundström, O. Forsén, M. H. Barker, *Electrochim. Acta* **2017**, *245*, 512-525.
[17] a) A. T. Marshall, S. Sunde, M. Tsypkin, R. Tunold, *Int. J. Hydrogen Energy* **2007**, *32*, 2320-2324; b) R. Tunold, A. T. Marshall, E. Rasten, M. Tsypkin, L.-E. Owe, S. Sunde, **2010**, *25*, 103-117.
[18] X. Wu, J. Tayal, S. Basu, K. Scott, *Int. J. Hydrogen Energy* **2011**, *36*, 14796-14804.
[19] a) E. Oakton, D. Lebedev, M. Povia, D. F. Abbott, E. Fabbri, A. Fedorov, M. Nachtegaal, C. Copéret, T. J. Schmidt, *ACS Catal.* **2017**, *7*, 2346-2352; b) M. Etzi Coller Pascuzzi, A. Goryachev, J. P. Hofmann, E. J. M. Hensen, *Appl. Catal. B Environ.* **2020**, *261*, 118225.
[20] a) M. Chatti, J. L. Gardiner, M. Fournier, B. Johannessen, T. Williams, T. R. Gengenbach, N. Pai, C. Nguyen, D. R. MacFarlane, R. K. Hocking, A. N. Simonov, *Nature Catal.* **2019**, *2*, 457-465; b) S. A. Bonke, K. L. Abel, D. A. Hoogeveen, M. Chatti, T. Gengenbach, M. Fournier, L. Spiccia, A. N. Simonov, *ChemPlusChem* **2018**, *83*, 704-710; c) M. Huynh, T. Ozel, C. Liu, E. C. Lau, D. G. Nocera, *Chemical Science* **2017**, *8*, 4779-4794.
[21] J. Kim, P. C. Shih, K. C. Tsao, Y. T. Pan, X. Yin, C. J. Sun, H. Yang, *J. Am. Chem. Soc.* **2017**, *139*, 12076-12083.
[22] Y. Lin, Z. Tian, L. Zhang, J. Ma, Z. Jiang, L. Chen, B. J. Deibert, R. Ge, *Nature Comm.* **2019**, *10*, 162-162.
[23] a) I. A. Moreno-Hernandez, C. A. Macfarland, C. G. Read, K. M. Papadantonakis, B. S. Brunschwig, N. S. Lewis, *Energy and Environmental Science* **2017**, *10*, 2103-2108; b) A. Shinde, R. J. R. Jones, D. Guevarra, S. Mitrovic, N. Becerra-Stasiewicz, J. A. Haber, J. Jin, J. M. Gregoire, *Electrocatal.* **2015**, *6*, 229-236.
[24] D. G. Brookins, *Chem. Geol.* **1986**, *54*, 271-278.
[25] a) J. P. Allen, J. J. Carey, A. Walsh, D. O. Scanlon, G. W. Watson, *J. Phys. Chem. C* **2013**, *117*, 14759-14769; b) B. Ouni, M. Haj Lakhdar, R. Boughalmi, T. Larbi, A. Boukhachem, A. Madani, K. Boubaker, M. Amlouk, *J. Non-Cryst. Solids* **2013**, *367*, 1-7; c) J. He, Y. Wei, T. Zhai, H. Li, *Materials Chemistry Frontiers* **2018**, *2*, 437-455.
[26] P. C. K. Vesborg, T. F. Jaramillo, *RSC Advances* **2012**, *2*, 7933-7947.
[27] a) B. Chen, S. Wang, J. Liu, H. Huang, C. Dong, Y. He, W. Yan, Z. Guo, R. Xu, H. Yang, *Corros. Sci.* **2018**, *144*, 136-144; b) J. Liu, T. Wang, B. Chen, *J. Electrochem. Soc.* **2019**, *166*, D798-D803.
[28] L. Zhou, A. Shinde, J. H. Montoya, A. Singh, S. Gul, J. Yano, Y. Ye, E. J. Crumlin, M. H. Richter, J. K. Cooper, H. S. Stein, J. A. Haber, K. A. Persson, J. M. Gregoire, *ACS Catal.* **2018**, *8*, 10938-10948.
[29] I. A. Moreno-Hernandez, B. S. Brunschwig, N. S. Lewis, *Energy and Environmental Science* **2019**, *12*, 1241-1248.
[30] T. A. Evans, K. S. Choi, *ACS Applied Energy Materials* **2020**.
[31] J. K. Yang, B. Liang, M. J. Zhao, Y. Gao, F. C. Zhang, H. L. Zhao, *Scientific Reports* **2015**, *5*, 1-6.
[32] C. Spöri, J. T. H. Kwan, A. Bonakdarpour, D. P. Wilkinson, P. Strasser, *Angewandte Chemie - International Edition* **2017**, *56*, 5994-6021.
[33] a) C. Costentin, D. G. Nocera, *Proc. Natl. Acad. Sci. U.S.A.* **2017**, *114*, 13380-13384; b) M. R. Mohammadi, S. Loos, P. Chernev, C. Pasquini, I. Zaharieva, D. González-Flores, P. Kubella, K. Klingan, R. D. L. Smith, H. Dau, *ACS Catal.* **2020**, *10*, 7990-7999; c) M. Huynh, D. K. Bediako, D. G. Nocera, *JACS* **2014**, 6002-6010.
[34] a) W. M. R. L. E. D. J. F. M. C. D. Wanger, G. E. Muilenberg, *Perkin-Elmer Corp.* **1979**; b) J. Matthew, *Surf. Interface Anal.* **2004**, *36*, 1647-1647.
[35] M. C. Biesinger, B. P. Payne, A. P. Grosvenor, L. W. M. Lau, A. R. Gerson, R. S. C. Smart, *Appl. Surf. Sci.* **2011**, *257*, 2717-2730.

[36] a) M. Sabri, H. J. King, R. J. Gummow, X. Lu, C. Zhao, M. Oelgemöller, S. L. Y. Chang, R. K. Hocking, *Chem. Mater.* **2018**, *30*, 8244-8256; b) R. K. Hocking, R. J. Gummow, H. J. King, M. Sabri, P. Kappen, C. Dwyer, S. L. Y. Chang, *ACS Applied Nano Materials* **2018**, *1*, 1603-1611; c) H. J. King, M. Fournier, S. A. Bonke, E. Seeman, M. Chatti, A. N. Jumabekov, B. Johannessen, P. Kappen, A. N. Simonov, R. K. Hocking, *J. Phys. Chem. C* **2019**, *123*, 28533-28549.
[37] H. Vincent, X. Turrillas, I. Rasines, *Mater. Res. Bull.* **1987**, *22*, 1369-1379.
[38] J. D. Donaldson, A. Kjekshus, D. G. Nicholson, T. Rakke, *Acta Chemica Scandinavica A* **1975**, 803-809.
[39] D. J. Morgan, *Surf. Interface Anal.* **2015**, *47*, 1072-1079.
[40] a) V. Kropáček, M. Krs, V. Bucha, *Studia Geophysica et Geodaetica* **1975**, *19*, 261-274; b) S. Ganguly, M. Kabir, B. Sanyal, A. Mookerjee, *Physical Review B - Condensed Matter and Materials Physics* **2011**, *83*, 2-5.
[41] a) S. D. Ghadge, O. I. Velikokhatnyi, M. K. Datta, P. M. Shanthi, S. Tan, P. N. Kumta, *ACS Applied Energy Materials* **2020**, *3*, 541-557; b) B. B. Xiao, X. B. Jiang, Q. Jiang, *PCCP* **2016**, *18*, 14234-14243; c) J. Greeley, J. K. Nørskov, *Electrochim. Acta* **2007**, *52*, 5829-5836.
[42] a) A. E. Russell, *PCCP* **2008**, *10*, 3607-3608; b) X. Lv, W. Wei, H. Wang, B. Huang, Y. Dai, *Appl. Catal. B Environ.* **2019**, *255*, 117743; c) L. Wang, A. Roudgar, M. Eikerling, *J. Phys. Chem. C* **2009**, *113*, 17989-17996.
[43] K. Kadakia, M. K. Datta, O. I. Velikokhatnyi, P. Jampani, S. K. Park, P. Saha, J. A. Poston, A. Manivannan, P. N. Kumta, **2012**, *37*, 3001-3013.
[44] Y. R. Luo, *CRC Press, Boca Raton* **2007**.
[45] a) J. Chen, A. Selloni, *Physical Review B - Condensed Matter and Materials Physics* **2012**, *85*, 1-9; b) P. W. Tasker, *Journal of Physics C: Solid State Physics* **1979**, *12*, 4977-4984; c) C. A. F. Vaz, H. Q. Wang, C. H. Ahn, V. E. Henrich, M. Z. Baykara, T. C. Schwendemann, N. Pilet, B. J. Albers, U. D. Schwarz, L. H. Zhang, Y. Zhu, J. Wang, E. I. Altman, *Surf. Sci.* **2009**, *603*, 291-297.
[46] S. P. Ong, L. Wang, B. Kang, G. Ceder, *Chem. Mater.* **2008**, *20*, 1798-1807.
[47] a) A. A. Eskandrani, S. M. Ali, H. M. Al-Otaibi, *International Journal of Molecular Sciences* **2020**, *21*; b) M. Suermann, T. J. Schmidt, F. N. Büchi, *Electrochim. Acta* **2018**, *281*, 466-471.
[48] M. A. Hubert, A. M. Patel, A. Gallo, Y. Liu, E. Valle, M. Ben-Naim, J. Sanchez, D. Sokaras, R. Sinclair, J. K. Nørskov, L. A. King, M. Bajdich, T. F. Jaramillo, *ACS Catal.* **2020**, *10*, 12182-12196.